Memoirs of the Faculty of Engineering, Nagoya University
Vol. 38, No. 2 (1986) — Research Report —

STABILITY OF FREE SHEAR LAYER

TOSHI FUJIWARA and TAKASHI KOIZUMI

Department of Aeronautical Engineering,

(Received October 31, 1986)

Abstract

A two-dimensional flow behind a splitter plate is solved using a numerical technique. Free shear layer is formed behind a splitter plate, when velocity difference is present upstream of the plate. An approach is attempted to observe the behaviors and stability of the flow. The flow properties are checked from a number of viewpoints, in order to see whether the numerical scheme and the calculated results are appropriate to express the real flowfield: The vortex pairing, the critical Reynolds number, the effect of viscosity, the distribution of Reynolds stresses etc. As a result, most of the important flow phenomena are both qualitatively and quantitatively reproduced in the solution at the Reynolds number lower than 10,000.

1. Introduction

In the present analysis, a mixing shear layer is studied using a finite difference method that is third-order accurate with respect to space and first-order accurate in time, originally given by Kawamura (Ref. 3). The first part of the study is reported in Ref. 17. where the calculation still needed improvements in connection with conservation of mass and the boundary condition on the splitter plate. Since our ultimate purpose is to treat a chemically reacting flow where mixing and combustion occur between fuel and oxidizer generally in a free shear region near injectors, a most simple shear layer behind a splitter plate is chosen as the present problem.

The purpose of the analysis is te solve incompressible Navier-Stokes equations as correctly as possible, to provide a number of features essentially observed in mixing shear layers without introducing a modeling, and to find out good relationships with the experimental observations by Brown and Roshko (Ref, 1), Dimotakis et al. (Ref. 2), Oguchi and Inoue (Ref. 4), Chih-Ming (Ref. 7) and Hussain et al. (Ref. 8).

The Kawamura scheme is used because of its third-order accuracy in space, even if it is not of conservation form, where the leading truncacion error term consists of the third-order mesh size multiplied by a fourth derivative (short-range diffusion term). By carefully constructing the grid system, this error term can be much smaller than viscous stress terms in Navier-Stokes equations, then yielding physically meaningful solutions.

Similar finite-difference analysis is done using the Quick method by Davis and Moore (Ref. 14) where thc flow is artificially perturbed to show vortex shedding; this is not necessary in the present numerical calculation. There are other finite-difference calculations successfully reproducing vortical structures in two-dimensional mixing shear layers (Refs. 9, 15). Interesting results are obtained by Jacobs and Pullin (Ref. 16) in a basic problem of vortex stretching and pairing. The vortex method is applied to the same mixing layer problem (Refs. 10-13), showing similar results to essentially inviscid flows.

The characteristics of the incompressible Navier-Stokes solutions are checked from various viewpoints: (i) Nonlinearity and linearity in applying the Kawamura scheme, (ii) implicit and explicit schemes, (iii) the influence of mesh size and truncation errors, (vi) coalescence of vortices, (v) comparison with inviscid solutions, (vi) transition Reynolds number, (vii) turbulence energy spectra, (viii) Reynolds stress, (ix) average velocity distribution (x) mass conservation and (xi) average third-order moments of fluctuating velocities. The effect of boundary conditions is also discovered quite essential to hold mass conservation throughout the flowfield.

2. Fundamental Equations

As to the entrance condition, a laminar boundary layer profile is assumed only until the entrance to the domain; the laminar boundary layers are assumed until L_0 upstream of the trailing edge of a splitter plate. Therefore, the splitter plate is extending to upstream, forming a Blasius-type velocity profile until the entrance to the computational domain, the downstream ot which is solved by the Navier-Stokes equations. Thus, the interaction between the upstream of the trailing edge and the downstream vortices can be introduced here.

The two-dimensional incompressible Navier-Stokes equations are given in the following form:

Mass; $$\nabla \cdot \boldsymbol{V}=0, \tag{1}$$

Momentum; $$\frac{\partial \boldsymbol{V}}{\partial t}+\boldsymbol{V}\cdot\nabla\boldsymbol{V}=-\nabla p+\frac{1}{R_e}\nabla^2\boldsymbol{V}, \tag{2}$$

where the physical quantities are non-dimensionalized by the following constants:

$$\begin{aligned} &\text{Characteristic velocity;} && U_0=|U_1-U_2|,\\ &\text{Characteristic length;} && x_0=y_0=L_0,\\ &\text{Characteristic time;} && t_0=L_0/U_0,\\ &\text{Characteristic pressure;} && p_0=\rho_0 U_0{}^2. \end{aligned} \tag{3}$$

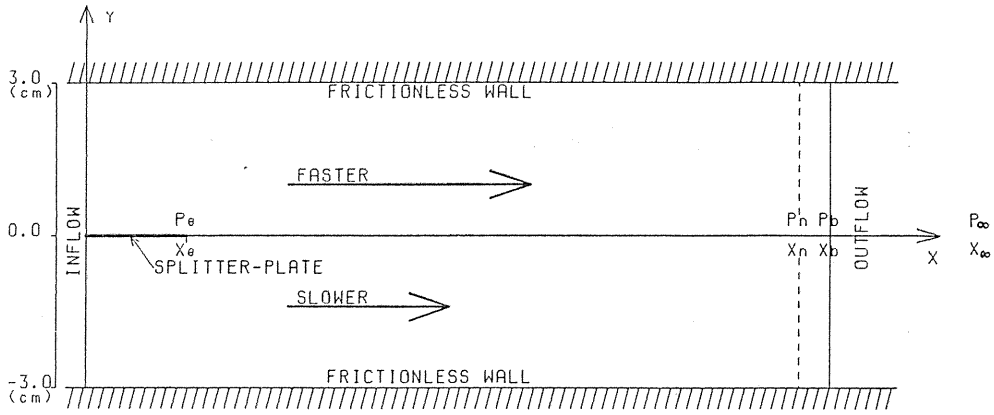

Fig. 1. The geometry of the flow and boundary conditions.

As shown in Fig. 1, the computational domain consists of a channel sandwiched by two frictionless walls (there is no interest in the wall boundary layers); 6 cm width×14.66 cm or 42.16 cm length. Out of the entire plate length, only the final $L_0=2.0$ cm sticks out into the computational domain. At the inlet, as mentioned adove, the flow is assumed to have velocity profiles of laminar Blasius boundary layer on both sides of the splitter plate. The whole length X of the plate is adjusted to yield a 0.5 cm-thick boundary layer at the inlet of the (upper) faster flow; for example, $X=15.1$ cm for $R_e=1577$ and $X=85.4$ cm for $R_e=10013$. Here the Reynolds number is defined as

$$R_e=\frac{\rho_0 L_0|U_1-U_2|}{\mu}, \tag{4}$$

where μ is the viscosity of air at STP.

According to the Kawamura method, the pressure field is solved using the following Poisson equation derived from Eqs. (1) and (2):

$$\nabla^2 p=-\mathrm{div}\ (\boldsymbol{V}\cdot\nabla\boldsymbol{V}). \tag{5}$$

The velocity field was solved by the Euler backward scheme in the original paper (Ref. 3), as shown in the difference equation

$$\frac{\boldsymbol{V}^{n+1}-\boldsymbol{V}^n}{\Delta t}+(\boldsymbol{V}^{n+1}\cdot\nabla)\boldsymbol{V}^{n+1}=-\nabla p+\frac{1}{R_e}\nabla^2\boldsymbol{V}^{n+1}, \tag{6}$$

where the convection term was linearized as

$$(\boldsymbol{V}^{n+1}\cdot\nabla)\boldsymbol{V}^{n+1}=(\boldsymbol{V}^n\cdot\nabla)\boldsymbol{V}^{n+1}. \tag{7}$$

In the present analysis. the following schemes are tested in order to find out the simplest method of calculation:

(a) Forward scheme (nonlinear convection term, explicit);

$$\frac{\boldsymbol{V}^{n+1}-\boldsymbol{V}^n}{\Delta t}+(\boldsymbol{V}^n\cdot\nabla)\boldsymbol{V}^n=-\nabla p+\frac{1}{R_e}\nabla^2\boldsymbol{V}^n. \tag{8}$$

(b) Backward scheme (nonlinear or linear convection term, implicit) ;

$$\frac{\mathbf{V}^{n+1}-\mathbf{V}^{n}}{\Delta t}+(\mathbf{V}^{n+1}_{n}\cdot\nabla)\mathbf{V}^{n+1}=-\nabla p+\frac{1}{R_e}\nabla^2\mathbf{V}^{n+1}. \tag{9}$$

After comparing these two schemes, it is found out that the expliclt method (8) is stable but not much faster, although the pressure field (5) is solved implicitly using the SOR method. In addition, the calculated vorticity field showed quantitative but no qualitative differences. Sensitivity of the flow to the inlet amd downstream boundary conditions is also different among such different versions of the Kawamura scheme.

The convection term is approximated by the following upwind scheme where the leading error term is of the order of h^3 × fourth derivatives:

$$\left(f\frac{\partial u}{\partial \xi}\right)_{i,j}$$
$$=\begin{cases} f_{i,j}(u_{i+2,j}-2u_{i+1,j}+9u_{i,j}-10u_{i-1,j}+2u_{i-2,j})/6\Delta\xi \text{ for } f_{i,j}\geqq 0, \\ f_{i,j}(-2u_{i+2,j}+10_{i+1,j}-9u_{i,j}+2u_{i-1,j}-u_{i-2,j})/6\Delta\xi \text{ for } f_{i,j}\leqq 0. \end{cases} \tag{10}$$

The utilized grids are shown in Figs. 2 (a) through (c), where the number of the mesh points is (a) 43×61 for the 6 cm×14.66 cm computational domain and (b) 43×181 for the 6 cm×42.16 cm domain. In fine mesh regions, the mesh size is less than 1 mm which corresponds to the dimensionless mesh $h=\Delta x/L_0<1/20$. Comparing the truncation error term with the viscous stress term with respect to order estimation, we find

$$h^3<1/R_e, \tag{11}$$

when $R_e<5000$. Thus the present grid system can resolve, only in the fine mesh regions, the viscous features of a flow with such a Reynolds number. In the following calculations, the Reynolds numbers are chosen $R_e=1588$ and 10013 from such reasons, although $R_e=10013$ slightly fails to satisfy the above inequality. The importance of this criterion (11) is justified by improving the spatial resolution; (c) the mesh number is increased to 85×122 for the 6 cm×14.66 cm domain. The essential flow characteristics remains unchanged, while snapshot flow patterns at fixed times are extremely altered. In order to increase the Reynolds number above 5000 and still retain quantitative accuracy in the calculated results, the mesh size has to be chosen smaller, resulting in the increase of computing time.

3. Detailed Method of Analysis

The boundary and initial conditions, stability, magnitude of errors and turbulence-related quantities are discussed before the calculated results are shown.

(a) Boundary conditions:

(a-1) Velocity:

On channel walls ($y=\pm 3$ cm) ; $du/dy=v=0$ (slip wall). (12)

At exit ($x=x_b=14.66$ or 42.16 cm) ;

$$du/dx=dv/dx=0. \tag{13}$$

At inlet ($x=x_0=0$ cm) ;

u and v are given by the Blasius profiles. (14)

The entire length X of the splitter plate is given by the condition that the displacement thickness of the upper boundary layer (faster side)

$$\delta=5\left(\frac{\mu[X-L_0]}{\rho_0 U_1}\right)^{1/2}=0.5 \text{ cm}.$$

Thus, the length X is given as a function of the Reynolds number R_e and the upper velocity U_1 :

R_e	U_1 (cm/sec)	X (cm)
95	12	2.8
1577	200	15.1
10013	1270	85.5

On splitter plate ($y=0$, $0<x<L_0=2$ cm) ; $u=v=0$. (15)

(a-2) Pressure:

On channel walls: $\partial p/\partial y=0$. (16)

At inlet: $\partial p/\partial x=0$ or $p=p_\infty=\text{const.}$ (17)

At exit ($x=x_b$) :

The following interpolation is used between one mesh before the boundary $x=x_n$ and $x=\infty$ ($x_\infty-x_n$ is approximated as x_b-x_e), where x_e=the trailing edge of the splitter plate:

$$p_b=p_n+\frac{x_b-x_n}{x_b-x_e}(p_\infty-p_n). \tag{18}$$

This is given by assuming that the pressure reaches p_∞ at $x=\infty$; p_b is calculated by linearly interpolating between p_n and p_∞(Ref. 3).

On splitter plate:

Since $u=v=0$ on the splitter plate, the Navier-Stokes equations give the following conditions on the pressure distribution;

$$\nabla p=-\frac{1}{R_e}\nabla^2 V \tag{19}$$

The Poisson equation (5) is solved under the boundary condition (19) as the Neumann condition.

(b) Initial conditions:

Since the present purpose is to generate an unsteady flow field, the resulting

flow is considered insensitive to initial conditions. Therefore, attention is focused on reducing computer time by imposing initial conditions as realistic as possible. Upstream of $x=2$ cm, the flow imposed at the inlet boundary is assumed, while at $x>2$ cm an artificial distribution is given; on the other hand the initial pressure is assumed uniform at $p=p_\infty$.

(c) Utilized grid systems:

High resolution is necessary in the vicinity of trailing edge and highly mixing regions, suggesting the use of adaptive grid systems. As such orthogonal and linear systems, the following is used:

$$x=A_1 e^{a_1\xi}-e^{-a_2\xi}+A_2,$$
$$y=A_3\sinh(a_3\eta), \tag{20}$$

where the coefficients a_1 through a_3 and A_1 through A_3 are chosen in three ways; (a) normal mesh 43×61 for $6\,\text{cm}\times14.66\,\text{cm}$ domain, (b) stretched only in the x direction, 43×181 for $6\,\text{cm}\times42.16\,\text{cm}$ domain, and (c) two-fold fine mesh, 85×122 for $6\,\text{cm}\times14.66\,\text{cm}$ domain.

As a special case. a finite-width splitter plate (thickness$=0.172$ cm) is also considered where the grid (a) is employed.

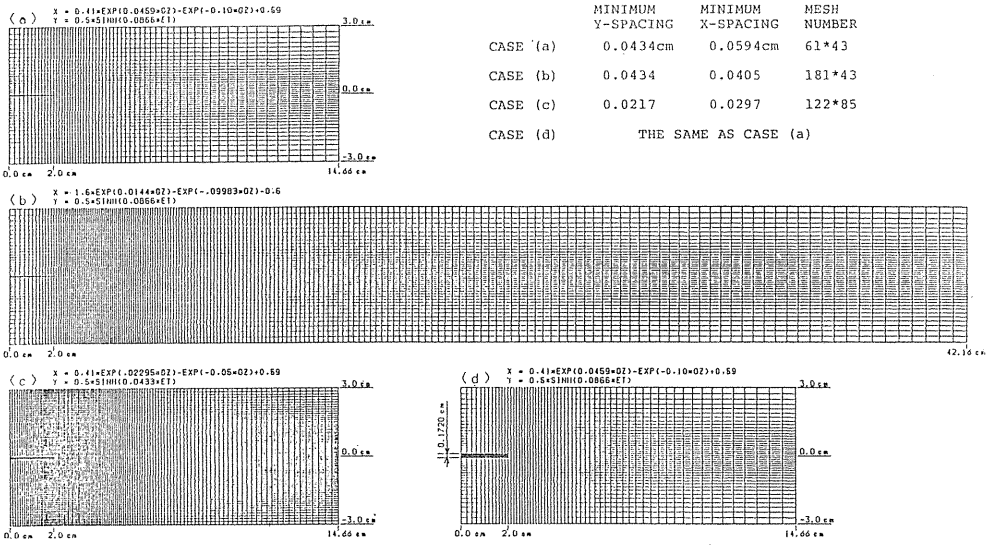

	MINIMUM Y-SPACING	MINIMUM X-SPACING	MESH NUMBER
CASE (a)	0.0434cm	0.0594cm	61*43
CASE (b)	0.0434	0.0405	181*43
CASE (c)	0.0217	0.0297	122*85
CASE (d)	THE SAME AS CASE (a)		

Fig. 2. The utilized grid systems: (a) Coarse, (b) long, (c) fine and (d) finite-width splitter plate in coarse mesh system.

(d) Pressure on splitter plate:

On the splitter plate; the pressure p_s is given by

$$p_s=p_{s\pm1}\pm\frac{\partial p}{\partial\eta}, \tag{21}$$

where $\partial p/\partial\eta$ is written as

$$\left.\frac{\partial p}{\partial \eta}\right|_s = -\frac{1}{R_e}\left\{\frac{1}{y_\eta}(-v_{s+3}+4v_{s+2}-5v_{s+1})-\frac{y_{\eta\eta}}{2y_\eta{}^2}(-v_{s+2}+4v_{s+1})\right\} \quad (22)$$

and + corresponds to the upper surface while − to the lower.

At the splitter edge, the value of the pressure is a three-valued function which is determined by the Eq. (5) from the three directions; above, right and below. Note that the pressure condition at this splitter edge must be of high accuracy because this condition is essential to trigger the generation of vortices in the downstream mixing layer region.

(e) Explicit and implicit schemes for velocity field:

The pressure field needs iterations because the Poisson equation must be solved by SOR, whereas there is a choice in the velocity field on whether an explicit or an implicit method is used.

When a forward difference is used, the seheme becomes am explicit scheme and the Navier-Stokes equations reduce to Eq. (8). Here the convection term has a nonlinear form. When the Euler backward difference is used, on the other hand, the scheme becomes implicit, as shown in Eq. (9), where the nonlinear convection term is either retained or linearized to check the effect of linearization. The solution of nonlinear implicit equations is acquired using the SOR technique for the flowfield as well.

(f) Reynolds stress and energy spectra:

The Reynolds stress and third-order moment of fluctuating velocities are typically defined as

$$-\rho\overline{(u'v')}_{i,j} = -\rho\left(\sum_{n_1}^{n_2} u'^n_{i,j}\cdot v'^n_{i,j}\right)/(n_2-n_1), \quad (23)$$

$$\overline{(u'v'^2)}_{i,j} = \left(\sum_{n_1}^{n_2} u'^n_{i,j}\cdot v'^n_{i,j}\cdot v'^n_{i,j}\right)/(n_2-n_1). \quad (24)$$

The energy spectra of fluctuating velocities defined by

$$E_{i,j}(\omega) = \frac{<\{u'_{i,j}(\omega)\}^2>}{\int_0^\infty <\{u'_{i,j}(\omega)\}^2> d\omega} \quad (25)$$

can be expressed by the Fourier transformation of the velocity fluctuations as

$$E_{i,j}(\omega_k) = \frac{N\Delta t}{2\pi}\frac{\left|\sum_{n=0}^{N-1} u'^n_{i,j} e^{-I\omega_k t_n}\right|^2}{\sum_{k=0}^{N-1}\left|\sum_{n=0}^{N-1} u'^n_{i,j} e^{-I\omega_k t_n}\right|^2}. \quad (26)$$

(g) Streakline defined by the trace of a marker particle:

Marker particles are placed along a vertical line at an upstream portion, thier subsequent motion being observed in a Lagrangian manner. The volocity $(u_p, ,v_p)$ of a marker particle at time $t=n\Delta t$ is interpolated dy the values of 4 neighboring points. Then the position of the marker particle at the next time step $t=(n+1)\Delta t$ is calculated by the following first-order formula:

$$\begin{aligned} x_p{}^{n+1} &= x_p{}^n + u_p{}^n\cdot\Delta t, \\ y_p{}^{n+1} &= y_p{}^n + v_p{}^n\cdot\Delta t. \end{aligned} \quad (27)$$

New marker particles are introduced in a similar manner at every several time steps to visualize the streaklines. In particular, the interface between the upper and lower fluids is well identified by streaklines, thereby enabling us to observe the feature of entrainment by the faster flow.

4. Results and Discussions

Computed results are examined from various aspects, to check whether the scheme and boundary conditions are correctly applied and whether the results possess necessary turbulence characters. Since some of the flow properties are already reported in Ref. 17 in detail, only subsequent progresses are mentioned here.

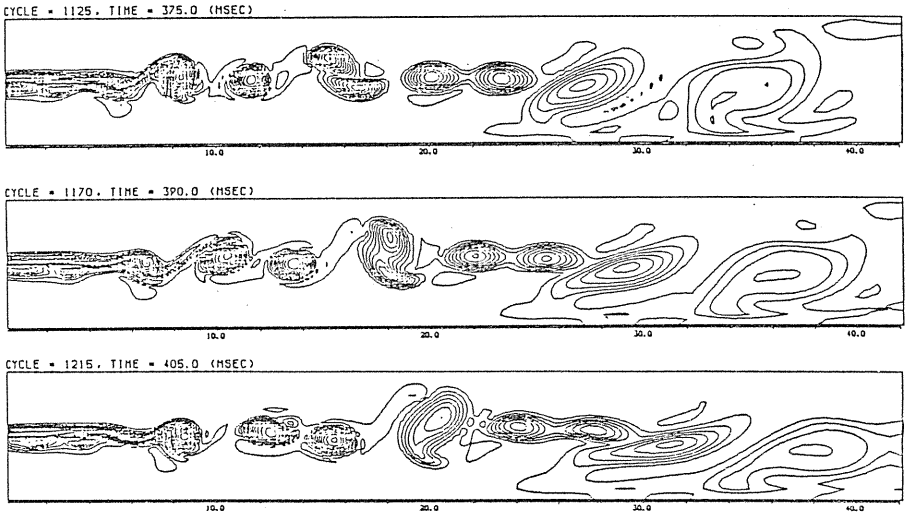

Fig. 3. Vorticity distribution at $t=375$, 390 and 405msec, for $R_e=1577$.

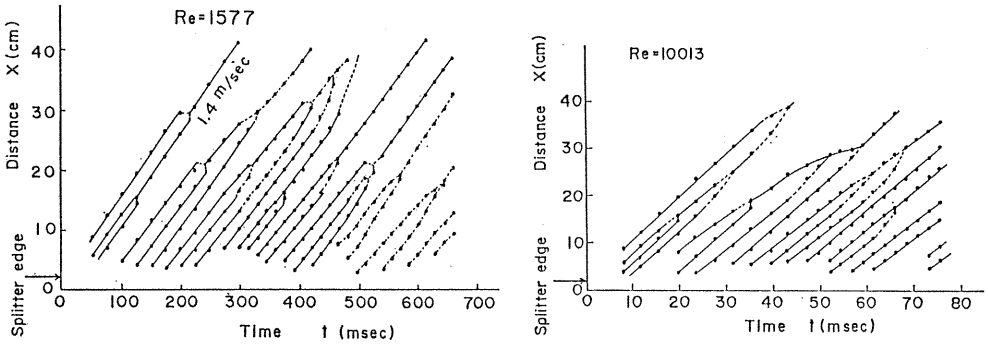

(a) (b)

Fig. 4. Distance-time diagram of vortices, their rollup and merging into larger ones, while convecting with nearly at a velocity averaged between faster and slower flows. (a) $R_e=1577$ ($U_1=2.0$ m/sec, $U_2=0.8$m/sec) and (b) $R_e=10013$ ($U_1=12.7$ m/sec, $U_2=5.08$m/sec).

(i) Development of vortical mixing layer: As shown in Fig. 3, the case of $R_e=1588$ shows the generation of vortices in the mixing shear layer region. The vortices are produced by the instability of the flow conceivably generated in the vicinity of the trailing edge of the splitter plate. In the downstream the pairing of two vortices occurs; two vortices come close and merge after rollup, generating a larger vortex. Such merging occurs in sequence, as shown in Fig. 4 and Ref. 1, reducing the total numder of vortices in the downstream. The convective velocity of the

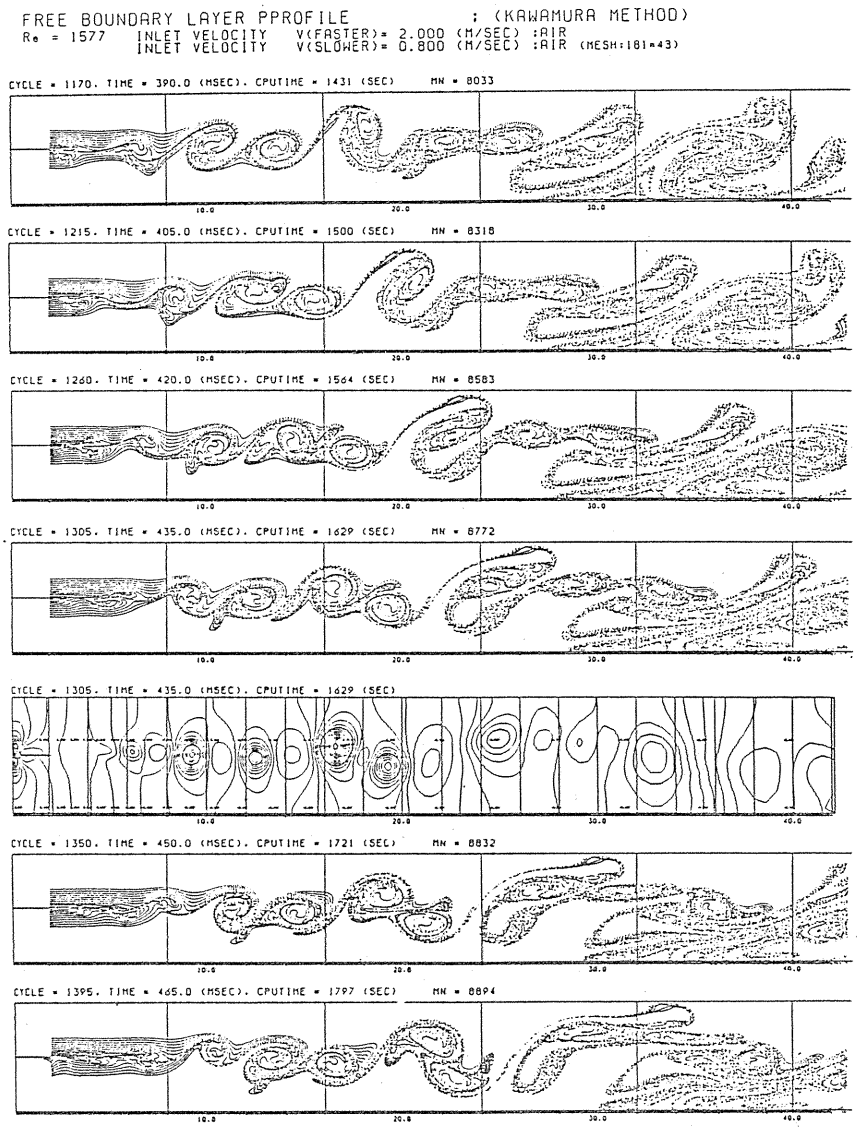

Fig. 5 Behaviors of streaklines between $t=390$ and 465 msec for $R_e=1577$. A pressure distribution is also shown at $t=435$ msec. Formation of new vortices, their merging, rollup and growth into a larger vortex are clearly seen.

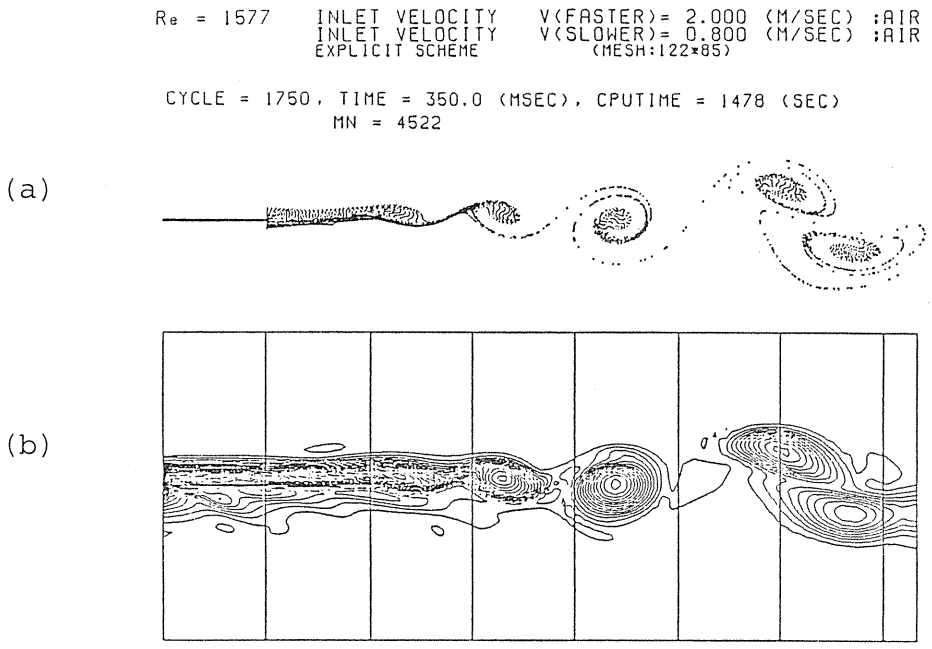

Fig. 6. Streakline and vorticity distributions at $t=350$ msec for $R_e=1577$. (a) Streakline and (b) vorticity show a good resemblance.

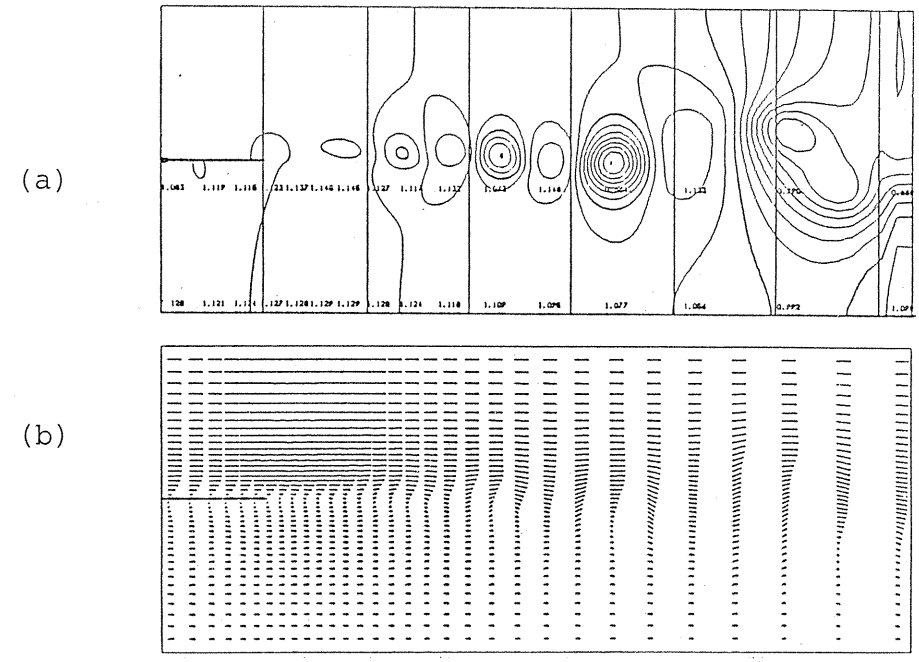

Fig. 7. Pressure and velocity vector distribution at $t=350$msec for $R_e=1577$. (a) Pressure and (b) velocity vector. Pressure shows a good agreement with streakline and vorticity shown in Fig. 6.

vortices naturally agrees with the average value between the upper and lower flow velocities.

A typical streakline behavior is shown in Fig. 5, where the entrainment of slower fluid by faster one is clearly seen, indicating a considerable increase of contact area between the two fluids. The distribution of pressure and vorticity tells the flow features more clearly because unlike streaklines the instantaneous flow patterns can be observed in it (Figs. 6 and 7).

(ii) Stability limit of flow: As a criterion to judge whether the flow is stable or not for a given Reynolds number, the temporal variation of the following quantities is monitored during the present calculation:

$$A_n=\left[\frac{\sum_{i=1}^{I}\sum_{j=1}^{J}(a_{i,j}^{n}-a_{i,j}^{n-1})^2}{I\times J}\right]^{1/2}\frac{0.02}{\Delta t}, \tag{28}$$

$$B_n=|a^n-a^{n-1}| \qquad (\text{at } x=14.66\text{ cm},\ y=0), \tag{29}$$

$$C_n=a^n-a^{n-1} \qquad (\text{at } x=14.66\text{ cm},\ y=0). \tag{30}$$

The results show that the centerline fluctuations B_n and C_n attenuate at $R_e=$

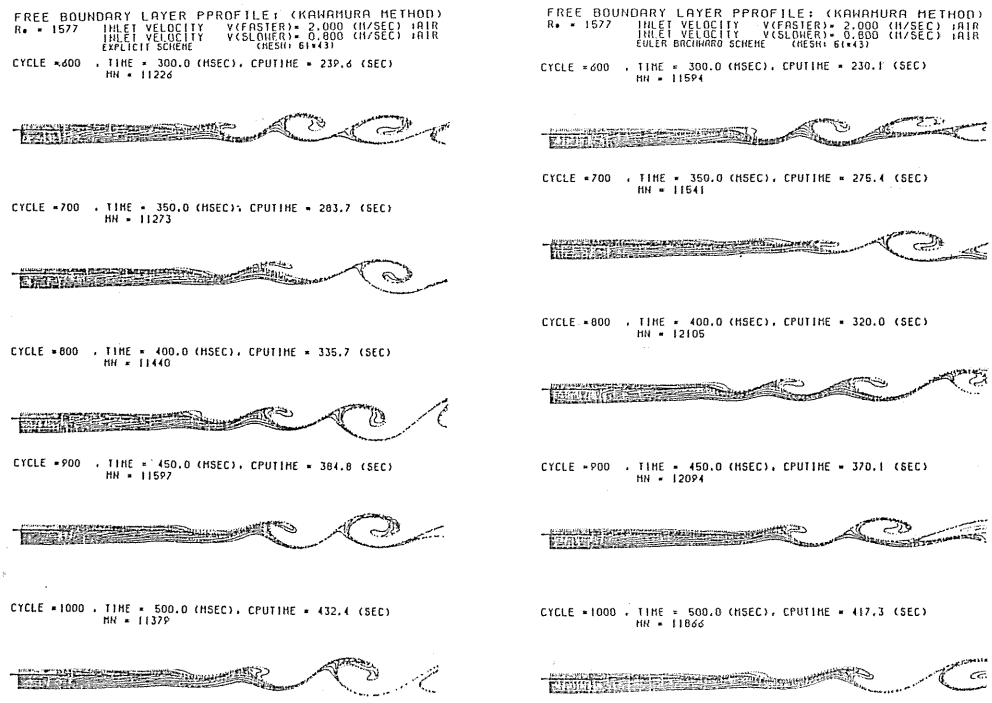

(a) (b)

Fig. 8. Comparison between explicit and implicit scemes of Kawamura method; R_e=1577, t=300~500 msec, coarse mesh in Fig. 2(a), U_1=2.0 m/sec and U_2=0.8 m/sec. (a) Explicit and (b) implicit.

197, while they amplify at $R_e=237$, indicating the critical Reynolds number between 197 and 237. On the contrary, the average per-mesh and per-step variation A_n shows attenuating tendency for any Reynolds numbers, and therefore is inappropriate as a criterion.

(iii) Stability of flow against artificial perturbation:

In agreement with the critical Reynolds number shown in (ii), the flow is found stable for $R_e=95$. In order to artificially disturb this stable flow from outside, sinusoidal velocity fluctuations with a frequency $0.625/t_0$ are applied at the channel entrance during $t=(3.0\sim6.2)\times t_0$. Although the flow yields a periodical oscillation in A_n only during the perturbed time interval, a rapid return to original stable state is observed thereafter.

(iv) Explicit and implicit schemes: By setting the Reynolds number at $R_e=1577$ and using the grid (a) in Fig. 2, the solutions are compared in Fig. 8. As shown in the streakline patterns, the explicit schcme shows more entrainment, wider mixing layer thickness and more extended vorticity distribution than the implicit one,while the pressure distribution behaves alike and the mass conservation throughout the flowfield is held quite accurately in both cases.

As to CPU time, there is not essential difference between both schemes, because most of computer time is spent for the pressure SOR which is implicit and necessitating 1 through 20 iterations (very rarely over 100 iterations).

Generally speaking, there are no essential differences between the explicit and implicit schemes, regarding the quality of results or economy of computing time.

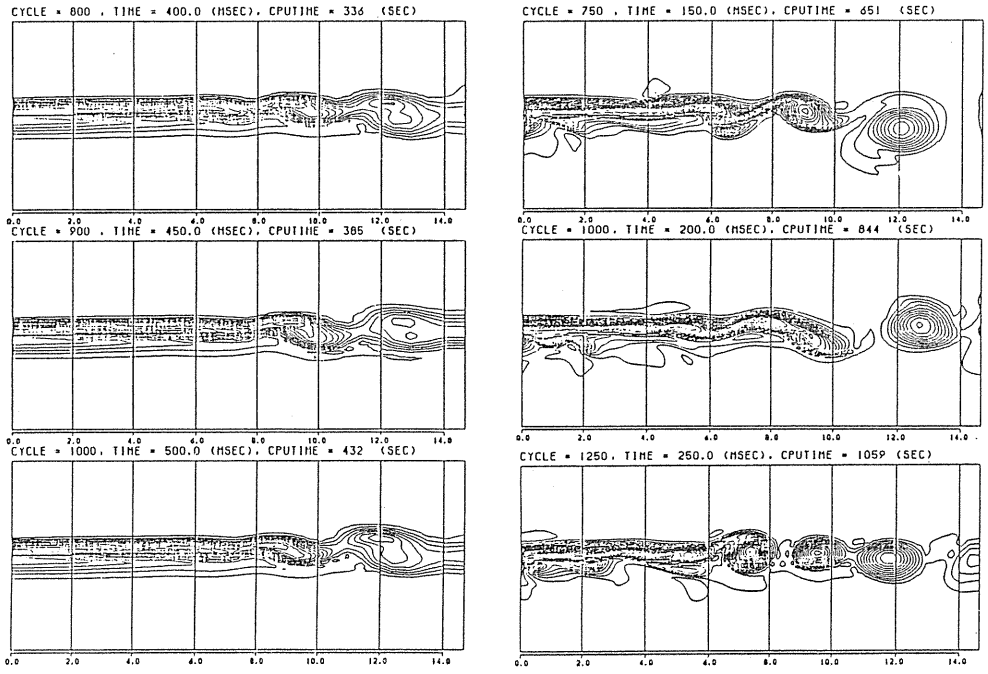

(a) (b)

Fig. 9. Comparison between coarse and fine grids; $R_e=1577$. (a) Coarse for $t=400\sim500$ msec, (b) fine for $t=150\sim250$ msec.

(v) Coarse and fine grids: The same calculation is performed using a coarse grid (a) and fine one (c) shown in Fig. 2. The results are compared in Fig. 9 where the fine mesh (c) gives much better resolution in vorticity. pressure, streakline and more conspicuous entrainment, due to one-order smaller truncation.

(vi) Constant-pressure boundary condition at inlet: From fundamental point of view, the Blasius velocity profile assigned at the inlet is consistent only with a constant pressure there. However, the calculated results show a number of unrealistic flow phenomena like large mass flow fluctuations, a strong pressure gradient near entrance, a longer distance of transition to vortical structure and the existence of small scale turbulence already near the trailing edge. It is considered that such strange behaviors are caused by imposing a constant pressure at the inlet and preventing the upstream propagation of presure disturbances generated by the motion of downstream vortices. In real experiments, in fact, it is hardly possible to maintain a constant pressure at the inlet as well.

(vii) Finite-width splitter plate: The thickness of the splitter plate is increased to 0.172 cm (two meshes). Although the boundary conditions are not elaborated on the splitter edge, the calculated flowfields are essentially unchanged from the case of infinitesimally thin splitter plate. This is due to the existence of much thicker boundary layers on the splitter plate, masking the effect of plate thickness.

5. Concluding Remarks

Through several examination procedures, the present finite difference method proved to be useful in computing mixing shear layers, because the calculation was able to provide nearly all the necessary characters of turbulent flows. In order to increase the accuracy of calculation, the mesh size must be reduced not only in the near wake, but also considerably in the far wake region.

It can be pointed out that starting from an initial condition a vortical flow structure was established without introducing artificial perturbations at the inlet, i. e. somewhat periodical vortex shedding processes were inherent to the imposed flow characters.

There is essentially no difficulty in extending the present calculation to a flow with compressibility, three-dimensionality and exothermic chemical reactions, although virtually numerical-diffusion-free schemes need to be used in handling strong gradients in concentrations and temperature existing in flames.

References

1) G. L. Brown and A. Roshko; On Density Effects and Large Structure in Turbulent Mixing Layers, J. Fluid Mech. Vol. 64, Part 4, 775 (1974).
2) P. E. Dimotakis, R. C. Miake-Lye and D. A. Papantoniou; Structure and Dynamics of Round Turbulent Jets, Phys. Fluids Vol. 26, 3185 (1983).
3) T. Kawamura and K. Kuwahara; Computation of High Reynolds Number Flow around a Circular Cylinder with Surface Roughness, AIAA Paper 84-0340, 1984.
4) H. Oguchi and O. Inoue; Mixing Layer Produced by a Screen and Its Dependence on Initial Conditions, J. Fluid Mech. Vol. 142, 217 (1984).

5) O. Inoue; Vortex Simulation of Turbulent Mixing Layer, ISAS RN-228, Institute of Space and Aeronautical Science, 1983.
6) F. F. Grinstein, E. S. Oran and J. P. Boris; Numerical Simulations of Asymmetric Mixing in Planar Shear Flows, NRL Memorandum Report 5621, 1985.
7) H. Chih-ming; Mixing Processes in Free Shear Layers, AIAA Paper 86-0234, 1986.
8) A. K. M. F. Hussain et al.; Free Shear flows: Organized Structures and Effects of Excitation. AIAA Paper 86-0235, 1986.
9) F. F. Grinstein, E. S. Oran and J. P. Boris; Direct Numerical Simulation of Axysymmetric Jets, AIAA Paper 86-0039, 1986.
10) J. L. Ellzey, J. W. Daily and D. S. Sherman; A Numerical Simulation of a Confined Mixing Layer Using the Random Vortex Method, AIAA Paper 86-0526, 1986.
11) A. F. Ghoniem and K. K. Ng; Effect of Harmonic Modulation on Rates of Entrainment in a Confined Shear Layer, AIAA Paper 86-0056, 1986.
12) N. N. Mansour and P. K. Barr; Simulation of Turbulent Mixing Layers, Sandia Report SAND84-8940, 1985.
13) N. N. Mansour; A Hybrid Vortex-in-Cell Finite-Difference Method for Shear Layer Computation, Sandia Report SAND84-8788, 1985.
14) R. W. Davis and E. F. Moore; A numerical study of vortex mixing in mixing layers, Phys. Fluids Vol. 28, 1626 (1985).
15) R. M. McInville, T. B. Gatski and H. A. Hassan; Analysis of Large Vortical Structures in Shear Layers, AIAA Journal Vol. 23, 1165 (1985).
16) P. A. Jacobs and D. I. Pullin; Coalescence of Stretching Vortices, Phys. Fluids Vol. 28, 1619 (1985).
17) T. Fujiwara, S. Taki and K. Arashi; Numerical Analysis of a Reacting Flow in Hydrogen-Oxygen Rocket Motor. Part 1: Analysis of Turbulent Shear Flow, AIAA Paper 86-0528, 1986.